

Deep Learning Based 3D Point Cloud Regression for Estimating Forest Biomass

Stefan Oehmcke
University of Copenhagen
stefan.oehmcke@di.ku.dk

Lei Li
University of Copenhagen
lilei@di.ku.dk

Jaime Revenga
University of Copenhagen
jar@ign.ku.dk

Thomas Nord-Larsen
University of Copenhagen
tnl@ign.ku.dk

Katerina Trepekli
University of Copenhagen
atr@ign.ku.dk

Fabian Gieseke
University of Münster
University of Copenhagen
fabian.gieseke@di.ku.dk

Christian Igel
University of Copenhagen
igel@di.ku.dk

Abstract

Knowledge of forest biomass stocks and their development is important for implementing effective climate change mitigation measures. It is needed for studying the processes driving af-, re-, and deforestation and is a prerequisite for carbon-accounting. Remote sensing using airborne LiDAR can be used to measure vegetation biomass at large scale. We present deep learning systems for predicting wood volume, above-ground biomass (AGB), and subsequently carbon directly from 3D LiDAR point cloud data. We devise different neural network architectures for point cloud regression and evaluate them on remote sensing data of areas for which AGB estimates have been obtained from field measurements in a national forest inventory. Our adaptation of Minkowski convolutional neural networks for regression gave the best results. The deep neural networks produced significantly more accurate wood volume, AGB, and carbon estimates compared to state-of-the-art approaches operating on basic statistics of the point clouds, and we expect this finding to have a strong impact on LiDAR-based analyses of terrestrial ecosystem dynamics.

1 Introduction

Forests provide resilience to climatic disturbances [NDB⁺07] and refuge for wildlife. They host about 80% of the terrestrial biodiversity and are major pillars of water and carbon cycles [TMMM09, AH11, HPM⁺13, CPB⁺06]. Forests, via photosynthesis, are consistent sinks of atmospheric CO₂ and have a higher rate of carbon storage than other ecosystems such as grasslands or agricultural

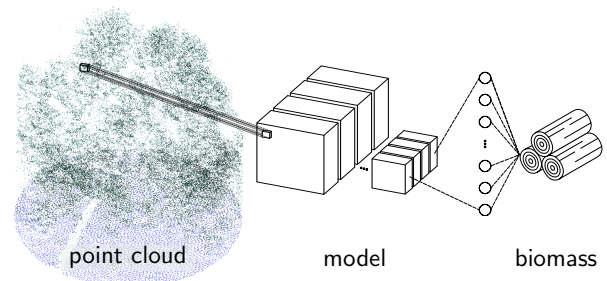


Figure 1: We use point cloud data from airborne LiDAR to estimate forest biomass and wood volume using deep learning.

lands [FTS⁺15, JHF17]. However, deforestation and forest degradation are causing much of this otherwise stored carbon to be released back into the atmosphere [LWMK19] highlighting the necessity to monitor the rapid changes of carbon stocks. A widely-used proxy for stored carbon is forest biomass [SM12]. Monitoring biomass dynamics is necessary for mitigation and adaptation measures against climate change due to the direct link to the global carbon cycle [Hou05]. Estimates of biomass is also needed to assess the resources available for the transition to green economy [LOH⁺11, KN17].

Above-ground biomass (AGB) measurements using remote sensing have been proved difficult to acquire accurately at high spatial resolution and at large scales [EKP⁺18, GAE⁺17]. These difficulties compromise effective mitigation strategies against long-term shifts in temperatures and weather patterns. Three different remote sensing techniques are currently applied to collect data used for AGB estimation: (1) synthetic aperture radar (SAR), (2) passive optical cameras,

and (3) light detection and ranging (LiDAR). In case of the latter, one can distinguish between spaceborne LiDAR, airborne laser scanning (ALS), and drone-based LiDAR. Biomass models derived from LiDAR data (regardless of the platform and range) usually prove a better performance than those derived from SAR or optical data [ZGD13]. Direct regressions of biomass using optical and SAR data tend to saturate with increasing AGB [MRMV+15, SJSN15, MSW+12]. Also, the quality of SAR data is very sensitive to differences in height (e.g., steep slopes or cliffs), while the quality of optical datasets is highly dependent on the absence of clouds in the region of interest [SJSN15]. Overall, LiDAR is a better-suited technology for monitoring the geometry over terrestrial ecosystems, mainly because: (a) it is an active sensor (it emits a light pulse that is sensed after reflection on the physical target) and (b) its laser characteristics (e.g., pulse wavelength) are more sensitive to slight differences in height and shape of vegetation. The state-of-the-art for predicting forest biomass from LiDAR point clouds is to voxelize the data (e.g., using $5 \times 5 \times 1$ m bins, where the vertical resolution is 1 m) and then to compute summarizing statistics of the point distribution along the vertical axis (e.g., maximum, median, and mean height) [LHC+99, MDAML11, MNLRN18]. These statistical features then serve as inputs to linear or power regression models for predicting forest biomass.

This study brings forward deep learning systems for improving the assessment of forest biomass based on 3D remote sensing data. In particular, we propose to apply deep neural networks directly to the point clouds (see Figure 1) instead of relying on models being based on simple statistical features. Our main contributions are as follows:

1. We study deep learning on point clouds for regression. This is an almost unexplored learning setting, except for the estimation of geometric properties from point clouds (e.g., pose-estimation [GRY18, FVA+21]). Furthermore, we consider data from airborne LiDAR (ALS), a technology with peculiarities [Næs09, GCC06] that produce more challenging point clouds than most standard benchmark data sets for 3D point cloud tasks. We adapted and compared three conceptually different deep neural network approaches [QSMG17, TQD+19, CGS19] for regression, finding that the regression based on Minkowski convolutional neural networks [CGS19] gave the best results for our tasks.
2. We show that predicting wood volume and in particular AGB of forest areas using deep learning can lead to considerably more accurate estimates compared to state-of-the-art and currently employed approaches operating on high-level statistics of the point distri-

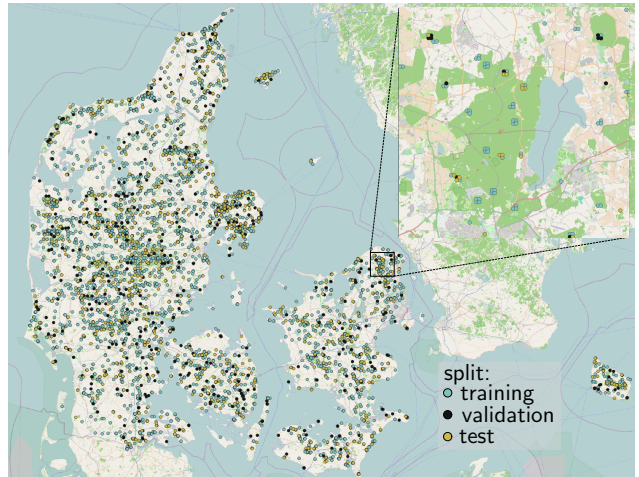


Figure 2: Measurement sites (Danish NFI plots). Color indicates how the data was split for training, validation, and testing (map background based on OpenStreetMap [Ope17]).

butions. This may pave the path for a paradigm shift for LiDAR-based analyses of terrestrial ecosystem dynamics.

The following section introduces our data, which combines field-based measurements with ALS point clouds. Afterwards, in Section 3, we present three conceptually different deep learning architectures from the literature and summarize the changes made to adjust them for point cloud regression. Section 4 describes the experiments including the baseline algorithms and the data set preparation. The results are presented and discussed in a broader context in Section 5 before we conclude in Section 6.

2 Forest Data

This section sketches how field studies obtain biomass (and thereby carbon stocks) as well as wood volume estimates in a systematic way for monitoring forests.¹ We also introduce the LiDAR data that are linked to these measurements.

Forest Inventory. The volume and biomass estimates used to train and evaluate our models stem from the Danish National Forest Inventory (NFI). The Danish NFI is based on a grid with cells of size 2×2 km covering the entire land surface of the country [NLJ16]. A plot composed of four circular subplots with a radius of 15 m, located in the corners of a 200×200 m square, is randomly placed within each grid cell. See Figure 2 for an overview of the

¹In this study, we consider data collected for Denmark, but our approach should be applicable for other areas in the world as well.

measurement sites. The full set of plots is geographically partitioned into five spatially balanced interpenetrating panels [Kis98, McD03, OSE+99, ZYTCS03]. Each year within a 5-year cycle, a different panel is measured, representing one fifth of the total set but representative of the entire country. Our data range from 2013 to 2017.

Each subplot is composed of three concentric circles with radii of 3.5 m, 10 m, and 15 m, respectively. Following standard procedures, a single caliper measurement of diameter is made at breast height (d_{bh}) (i.e., 1.3 m from the ground) for all trees in the 3.5 m circle. Trees with d_{bh} larger than 10 cm are measured in the 10 m circle, and only trees with d_{bh} larger than 40 cm are measured in the 15 m circle, see Figure 3 for an illustration. For a random sub-sample of 2-6 trees, further measurements of total height (h), crown height (h_c), age, and diameter at stump height (d_{st}) are obtained.

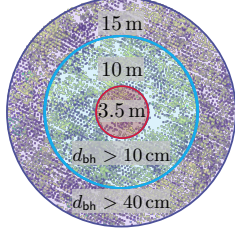


Figure 3: Subplot corresponding to a single input point cloud.

Based on the sub-sample measured for both h and d_{bh} , models are developed for each species and growth region. These functions use the observed mean height and mean diameter on each subplot for creating localized regressions using the approach suggested by Sloboda *et al.* [SGM93]. For subplots where no height measurements are available, generalized regressions are developed based on a modified Näslund-equation [Näs36, Joh99]. Subsequently, individual tree volume and biomass are estimated using species-specific models [NLMS17]. As the trees are measured in different concentric circles depending on their diameter, the growing stock volume and biomass on each subplot is estimated by scaling the individual tree estimate according to the circular area in which the tree has been measured.

In this study, we are interested in predicting the forest biomass and wood volume as well as the stored carbon, where the latter is considered to be a linear function of the biomass and was therefore not a separate regression target. Figure 4 shows the distribution of the regression targets in the test data set considered in our study. Throughout this article, biomass and carbon storage are measured in Mg (metric ton) per ha and volume in $\text{m}^3 \text{ha}^{-1}$.

Point Cloud Data. Airborne LiDAR point cloud data from across Denmark is publicly available from the Danish Agency for Data Supply and Efficiency.² The average resolution of the point clouds is 4.5 points per m^2 . Vertical and horizontal point accuracy is reported as root mean square error (RMSE), which is about 5 cm and 15 cm, re-

²<https://dataforsyningen.dk>

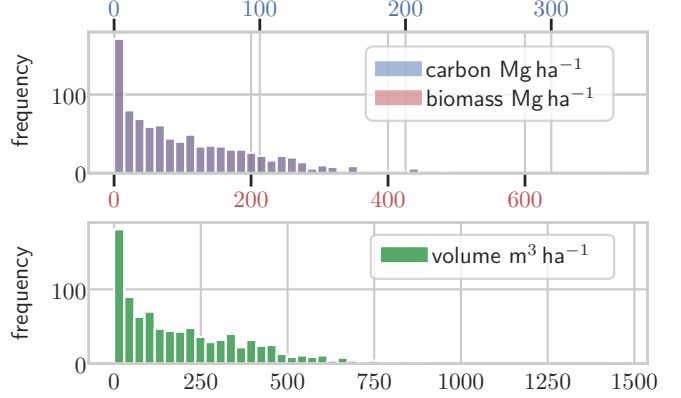


Figure 4: Histogram of the regression targets in the test set. Note that biomass and carbon overlap completely since the carbon estimate is computed as a linear function of the biomass.

spectively. From these data, the point clouds corresponding to the subplots studied in the NFI were extracted (see Figure 5). We acquired data ranging from 2014 to 2018. The average number of points per subplot is 11 684.35 with a standard deviation of 6743.81.

3 Deep Learning for Point Cloud Regression

From a mathematical perspective, a single point cloud can be represented via a set $\mathcal{P} = \{\mathbf{x}_1, \dots, \mathbf{x}_{n_{\mathcal{P}}}\} \subset \mathbb{R}^N$, where $n_{\mathcal{P}}$ is the number and N the dimensionality of the points (typically, $N = 3$). Besides these coordinates, additional information is often provided for each point, such as color or intensity. These features paired with the points define the set

$$\mathcal{P}_{\mathcal{F}} = \{(\mathbf{x}_1, \mathbf{f}_1), \dots, (\mathbf{x}_{n_{\mathcal{P}}}, \mathbf{f}_{n_{\mathcal{P}}})\} \subset \mathbb{R}^N \times \mathbb{R}^D \quad (1)$$

with $\mathbf{f}_i \in \mathbb{R}^D$ containing the additional features. Such a point cloud is given for each instance (e.g., one subplot corresponds to one point cloud, see Figure 5). The point cloud sets typically have different cardinalities and are unordered. Accordingly, the output of a model should not depend on the order of the provided points, a property referred to as permutation invariance. Furthermore, the spatial structure of such point clouds can be highly irregular and the density of points is typically very sparse (these characteristics usually vary among different regions as well).

Compared to deep convolutional neural networks (CNNs) for standard 2D and 3D images, the research field of deep learning for point cloud data has yet to mature. There are several approaches for adapting neural networks for point cloud processing, differing

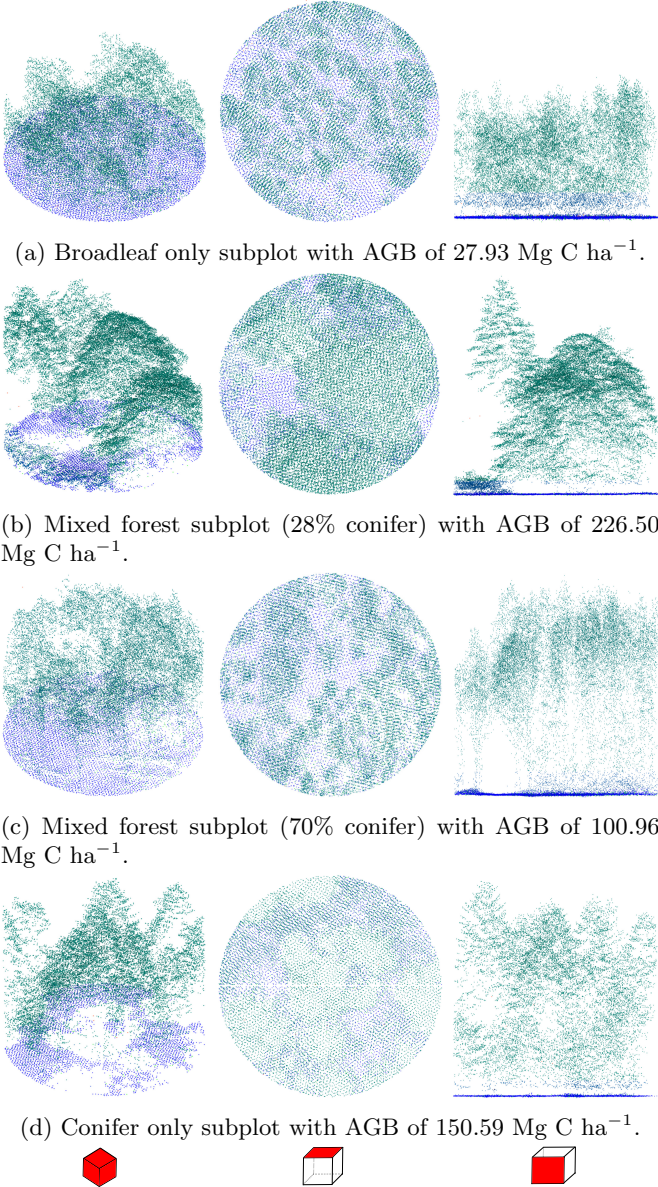


Figure 5: Examples of subplots with different fractions of broadleaf and conifer trees. Green and blue indicate points classified belonging to trees and ground, respectively. We show three perspectives: isometric front, top, and side view.

among others in how they deal with the key questions of how to extend the concept of spatial convolutions to sparse point clouds. Most deep learning systems for point clouds are developed for segmentation and other classification tasks [HSL⁺17, CFG⁺15, WSK⁺15]. In this study, we focus on regression tasks. We adapt and compare three widely-used and conceptually different point cloud classification approaches for regression: the classic PointNet [QSMG17], the kernel point convolution

(KPCConv) [TQD⁺19], and a Minkowski CNN [CGS19].

In the following, we briefly review the different architectures and describe how we used them for regression. We extended the open-source library TorchPoints3D [CNHL20] to support regression and will contribute our networks to the library upon acceptance of this manuscript.

3.1 PointNet

The seminal PointNet is one of the first deep learning architectures developed for point clouds [QSMG17]. PointNet-type networks apply the same feature map to each input point. The feature map is defined by a shared (dense) neural network. The original architecture is based on the use of multiple such neural network blocks. In between these blocks, input/feature transformations are used to align the data via learnable transformation matrices. At the end, to facilitate a variable number of points and to achieve permutation invariance, a symmetric set function is applied, which can be simply a max-pooling operation. Two PointNet variants have been proposed in the seminal work to address classification and segmentation scenarios, respectively.

To adapt the architecture for regression, we adopted the classification PointNet architecture up to the global feature aggregation. We then replaced the subsequent two hidden fully-connected layers (output dimensionalities: 512-256) with three fully-connected layers (output dimensionalities: 512-256-128) and considered a final linear output layer.

3.2 KPCConv

The *kernel point convolution* [TQD⁺19] extends standard discrete convolution to the domain of point clouds. Kernel point convolutions consider, for a given input point $\mathbf{x} \in \mathbb{R}^N$, a local neighborhood along with points called kernel points that are used to define a convolution operator. More precisely, the convolution of $\mathcal{P}_{\mathcal{F}}$ by a kernel g at a point $\mathbf{x} \in \mathbb{R}^N$ is defined via

$$(\mathcal{P}_{\mathcal{F}} * g)(\mathbf{x}) = \sum_{(\mathbf{x}_i, \mathbf{f}_i) \in \mathcal{N}_{\mathbf{x}}} g(\mathbf{x}_i - \mathbf{x}) \mathbf{f}_i . \quad (2)$$

Here $\mathcal{N}_{\mathbf{x}} = \{(\mathbf{x}_i, \mathbf{f}_i) \in \mathcal{P}_{\mathcal{F}} \mid \|\mathbf{x}_i - \mathbf{x}\| \leq r\}$, where $r \in \mathbb{R}^+$ is a hyper-parameter defining the domain $\mathcal{B}_r^N = \{\mathbf{y} \in \mathbb{R}^N \mid \|\mathbf{y}\| \leq r\}$ of the kernel g . The kernel g is based on a set $\{\tilde{\mathbf{x}}_1, \dots, \tilde{\mathbf{x}}_K\} \subset \mathcal{B}_r^N$ of K kernel points, where each kernel point $\tilde{\mathbf{x}}_k$ has an associated weight matrix $W_k \in \mathbb{R}^{D_{\text{in}} \times D_{\text{out}}}$, which maps a feature vector $\mathbf{f} \in \mathbb{R}^{D_{\text{in}}}$ to a new feature vector $\mathbf{f}' \in \mathbb{R}^{D_{\text{out}}}$ (for the first such convolution layer, we have $D_{\text{in}} = D$). One option for the kernel g :

$\mathcal{B}_r^N \rightarrow \mathbb{R}^{D_{in} \times D_{out}}$ is

$$g(\mathbf{y}) = \sum_{k=1}^K h(\mathbf{y}, \tilde{\mathbf{x}}_k) W_k, \quad (3)$$

where $h = \max(0, 1 - \frac{\|\mathbf{y} - \tilde{\mathbf{x}}_k\|}{\sigma})$ and $\sigma \in \mathbb{R}^+$ is a user-defined model parameter [TQD⁺19]. Thus, the kernel yields a weighted sum of weight matrices and each kernel is parameterized by its own kernel points and the corresponding weight matrices. The weight matrices are learnt similarly to the coefficients of convolution operators in standard CNNs. The kernel points can either also be learnt (“deformable”) or can be fixed (“rigid”) systematically around the center of \mathcal{B}_r^N [TQD⁺19]. Pooling operations are realized via creating a 3D grid in which all points in a cell are aggregated (see Section 3.3).

We adapt the KPConv architecture proposed for classification (KP-CNN) to utilize it for regression. KP-CNN follows the structure of ResNet, thus modifying it for regression was straight forward and was achieved by changing the output layer to have the identity as activation function. We resorted to fixed kernel points as deformable ones did performed better on our dataset.

3.3 Minkowski Convolutional Neural Network

A straight-forward approach to process point clouds is to voxelize the points to a 3D image (with D channels) and to apply a standard 3D convolutional neural network (CNN) to the resulting image. This requires binning, but while a coarse binning may discard important information, a fine-grained binning can render the computations intractable. However, the points are typically very sparse in 3D space. This lends to keeping a sparse representation and applying spatially sparse 3D convolutions, which basically operate only in areas where points exist [Gra15, GEVDM18]. A state-of-the-art implementation of sparse convolutions for 3D point clouds is given by the Minkowski Engine, an auto-differentiation library, which allows to efficiently implement standard architectures, such as ResNet with 3D convolutions [CGS19].

Both the Minkowski and KPConv architectures progressively downsample the point cloud based on a 3D grid via pooling operations. The initial grid size is only bound to the horizontal and vertical accuracy of the point data, which can result in a grid that might be too fine to be processed efficiently. Therefore, it is crucial to set the initial grid size according to the data and task. The subsequent pooling steps are then based on this initial size and work similarly to standard 2D pooling operations. Once a grid is created, a voxel-based approach, such as Minkowski CNNs, aggregates all voxels within a grid cell to a new voxel. In contrast, KPConv takes the mean

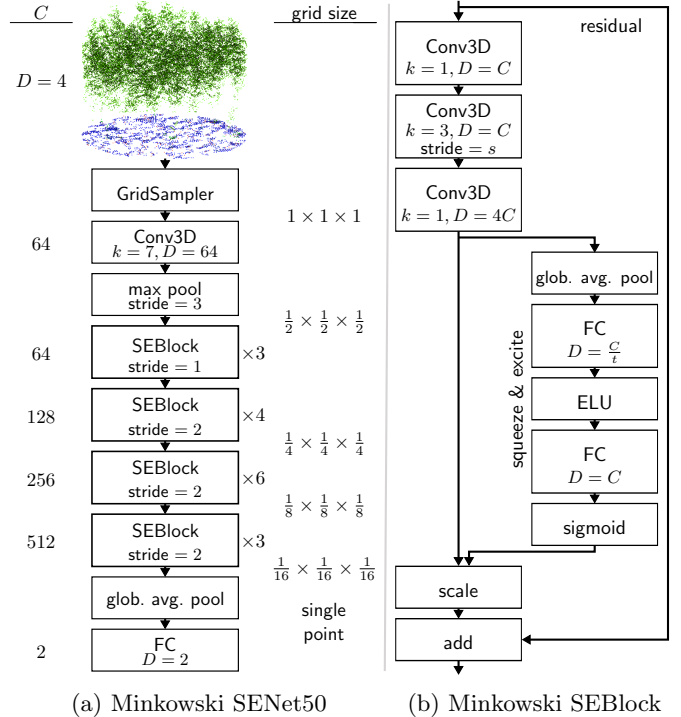


Figure 6: The implemented Minkowski SENet50 architecture is shown in (a). The grid is initialized by the GridSampler given an initial grid size, which the subsequent grid sizes are relative to. Conv3D depicts sparse 3D convolution with D channels followed by ELU activation and batch normalization. The kernel size k and stride is given as single number but extend to all three dimensions (e.g., $3 = 3 \times 3 \times 3$). FC layers are fully connected layers with hidden dimensionality D . (b) presents the bottleneck block. A block is configured by its input size C , stride s , and reduction rate t (defaults to 16).

of the position of all points within a cell to form a new point. By doubling the size of the grid cells in each subsampling/pooling layer, the number of points/voxels is incrementally reduced, which corresponds to increasing the receptive field size. The features associated with each new point can be obtained, for example, via max-pooling (applied to the feature vectors of the pooled points) or by applying the chosen convolution operator.

Using the Minkowski Engine library, we build a 3D version of SENet50 [HSS18] for regression, see Figure 6. To that end, we replaced 2D convolutions with their 3D equivalent. The stride of the initial convolution of SENet was changed from 2 to 1 in order to avoid early loss of information. We also replaced Rectified Linear Unit (ReLU) activation functions with Exponential Linear Units (ELU) [CUH16]. Finally, the output layer was changed to fit the number of target variables and does not apply a non-linear activation.

4 Experiments

The estimation of biomass based on point cloud data has, so far, been based on simple models operating on statistical features derived from the point clouds. In this section, we describe our experimental comparison of the three neural network architectures described in Section 3 with a previously used power regression approach as well as linear regression and random forest models using pre-computed features as baselines.

4.1 Data

We considered the dataset described in Section 2. Several preprocessing steps were conducted for both the deep neural networks (operating on the point clouds) as well as for the baselines that operate on simple statistical features. We describe these steps below as well as the statistical features used for the baselines.

4.1.1 Preprocessing

The forest data from the NFI include four error flags. The first error flag indicates whether there are trees visible in the point cloud that do not belong to the field-based measurements, while the second error flag marks whether any non-forest objects—such as land-lines or buildings—are part of the point cloud. We chose not to exclude these data since a method that directly works with the point cloud should detect irrelevant parts by itself, meaning that some previously excluded data should now be usable. The third error flag signals if the biomass was harvested in-between biomass measurements and airborne point cloud acquisition. Finally, the last error flag indicates unreasonable values. Since the third and fourth error flags are intractable, we excluded the marked samples accordingly.

In addition, we removed all samples with no points above 1.3 m as this is the minimal height considered for the biomass measurements.³ The remaining set consisted of $M = 6101$ individual point clouds, each being labelled with a corresponding biomass measurement as explained in Section 2. The biomass and wood volume were measured at different times than the collection of point clouds. To ensure that both data sources fit to another, we only considered point clouds that were within one year of the biomass measurement for our validation and test set. For training, we did consider larger temporal gaps (up to nine years) and added the time interval in years as a feature. Since some sites were measured multiple times, we kept measurements from the same site together in either

³Keeping these samples would have simply reduced the errors, because they could have been handled by a simple rule that predicts zero if the maximum height is below 1.3 m.

training, validation, or test split (i.e., no site/plot considered during training or for validation occurred in the test set).

Finally, to train, validate and test all the models, we split the data as follows: the training set contained 3232 samples with a time interval of more than one year and 1039 samples with an even longer time interval (i.e., 4271 training samples in total). The validation set consisted of 919 and the test sets of 911 samples with a maximum distance of one year between paired point cloud and biomass measurements.

4.1.2 Point Cloud Feature Extraction

The baselines considered, which are used for biomass estimation, rely on precomputed features from the height distribution in accordance with Nord-Larsen *et al.* [NLRNO17]: mean height, height standard deviation, coefficient of variation, skewness, kurtosis, percentiles of the height distribution (5th, 10th, 25th, 50th, 75th, 90th, 95th, 99th), and the interception ratio (IR), which is the fraction of points above one meter compared to all first returns. For each point cloud sample, these features except IR were computed twice, once for all points and once only for the points 1 m above ground.

The laser pulses from LiDAR hit objects at different heights above ground. Each pulse leads to one or several reflections received by the sensor, which are grouped in *returns*. The first return may come from the highest treetops and the last return from the ground. Complex surfaces may produce several returns, while from a flat surface only one return would be expected. Up to five returns were recorded for each measurement in our dataset, but we only considered the first returns for computing the features as done by Magnussen *et al.* [MNLRN18]. This gave better results in preliminary experiments than using all returns (in contrast, the deep learning methods simply use all returns). Overall, $d = 28$ statistical features were extracted per point cloud sample.

4.2 Experimental Setup

We conducted a detailed comparison of all methods for predicting AGB (and thereby above-ground carbon) and wood volume. We used the root-mean-square-error (RMSE), the coefficient of determination R^2 , and the mean absolute percentage error (MAPE) as evaluation metrics, in accordance with the related literature.

4.2.1 Linear and Power Regression

The first two baselines are based on linear regression and power regression models. For the linear regression models, all the d features were used as explanatory variables. The multivariate power regression can

be regarded as the state-of-the art for predicting AGB, above-ground carbon, and tree volume from the point cloud features [MNLRN18]. Following Magnussen *et al.* [MNLRN18] study, we fitted models of the form

$$y = w_1 \cdot z_{\text{mean AG}}^{w_2} \cdot z_{95^{\text{th AG}}}^{w_r} \cdot \text{IR}^{w_4} \quad (4)$$

for each quantity of interest. Here, $z_{\text{mean AG}}$ is the mean height of the points one meter above ground, $z_{95^{\text{th AG}}}$ is the 95th percentile of the height distribution of point one meter above ground, and IR is the inception ratio. For each model, the parameters $w_1, \dots, w_4 \in \mathbb{R}$ were set to the optimal least-squares estimates.

4.2.2 Random Forest

We trained random forest (RF) models with 5000 trees [Bre01] and resorted to the popular Scikit-Learn implementation [PVG⁺11]. The out-of-bag (OOB) error was used to tune the RF hyper-parameters. We considered $\{0.1, 0.2, \dots, 1\}$ for the ratio of features to consider at every split, $\{0.1, 0.2, \dots, 1\}$ for the ratio of samples to consider for each tree, $\{5, 6, \dots, 20, \infty\}$ for the maximum tree depth, and $\{1, 2, 4, \dots, 16\}$ for the minimum number of samples required at each leaf node. The best model used 90% of the features at every split, 20% of the training data for each tree, had a maximum depth of 11, and required a minimum number of 6 samples at each leaf node.

4.2.3 Neural Networks

Three different neural network architectures were applied: the proposed regression versions of PointNet, KPConv, and a 3D version of SENet50 [HSS18] build with the Minkowski Engine. All code was written in Python and PyTorch [PGM⁺19]. The positions of the input points are given in world coordinates. We centered the x - and y -coordinates for each subplot individually and scaled them by dividing by 15 m so that they lie within $[-1, 1]$. Since the ground points are already set to 0, centering the z -axis was not necessary.

We tuned the initial grid size of KPConv and the Minkowski model by gradually decreasing it (meaning increasing the spatial resolution) until no improvement could be seen on the validation set. Both architectures worked best with the initial grid size set to 0.025.

To increase diversity in the training set, several augmentations were considered. First, a random rotation around the z -axis was applied. We did not consider rotating the x - and y -axis since a tilt would result in unrealistic samples (e.g., change of growth direction). Thereafter, random dropout of points with a dropout rate of 20% in the 50% of all samples was applied, which increases variety and simulates changes in point density. Finally, each

Table 1: Comparison of methods showing the R^2 score, RMSE, and MAPE on the test set. The R^2 and MAPE for biomass are the same as for carbon. Note that we excluded 0 biomass measurements from MAPE to avoid numerical issues. Best results are highlighted.

target	model	R^2	RMSE	MAPE
AGB	lin. model	0.757	49.882	577.777
	power model	0.761	49.521	309.575
	RF	0.751	50.470	990.243
	PointNet	0.805	44.673	544.333
	KPConv	0.812	43.895	292.490
	Minkowski	0.826	42.250	106.797
volume	lin. model	0.760	93.516	172.907
	power model	0.763	92.852	213.230
	RF	0.755	94.375	222.817
	PointNet	0.800	85.385	146.718
	KPConv	0.804	84.561	81.505
	Minkowski	0.823	80.323	60.391

dimension of the point position was shifted by adding a small random value drawn from a zero-mean truncated Gaussian distribution with variance 0.001 and support $[-0.05, 0.05]$.

In addition to the coordinates of the points, we also provided our model with supplementary features. For each point, we appended the total number of returns of the laser pulse as well as the return of the point (see Section 4.1.2) and its height, since it is an important part of feature extraction methods. As global feature, we attached the time interval between NFI measurement and point cloud retrieval. This accumulates to a total of four additional features.

We employed the AdamW [LH19] optimizer with weight decay set to 0.01. The initial learning rate was 0.001, which was adapted according to the cosine annealing schedule with warm restarts ($T_0 = 10, T_{\text{mult}} = 2$) [LH17] for 310 epochs. The batch size was 32 and the smooth L1 function [Gir15] was used as training loss. These hyper-parameter configurations were chosen based on the highest R^2 score on the validation set.

5 Results and Discussion

An overview of our results is given in Table 1 showing the RMSE, R^2 , and MAPE for the different algorithms on the test set, which was not used for model development. Overall, the Minkowski model achieved the best results with an R^2 of 0.826 for biomass (and carbon storage) and an R^2 of 0.823 for wood volume. The corresponding RMSEs were 42.25 Mg ha^{-1} and 80.323 $\text{m}^3 \text{ha}^{-1}$, respectively.

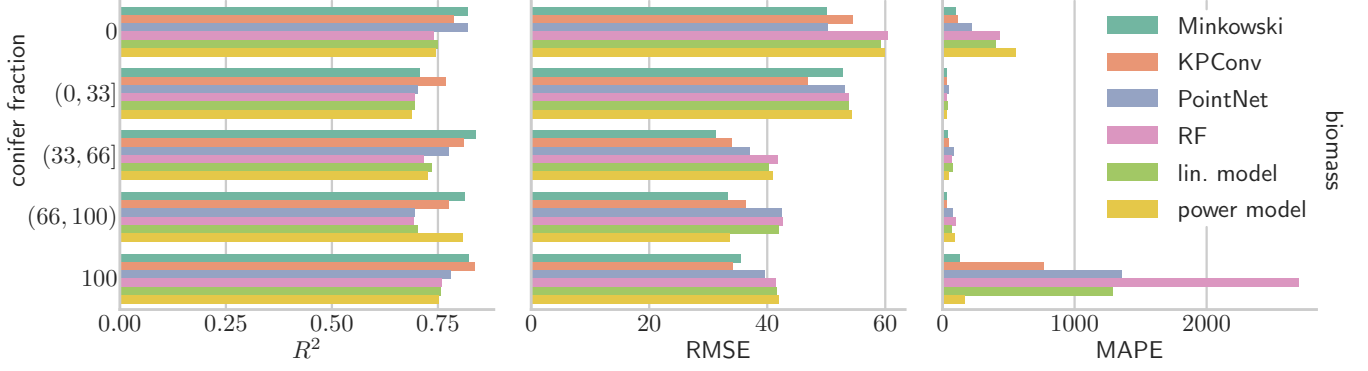


Figure 7: Errors for different fractions of conifer and broadleaf trees for biomass. The columns show R^2 , RMSE, and MAPE. The corresponding figure for wood volume can be found in the supplementary material (see Figure A.1).

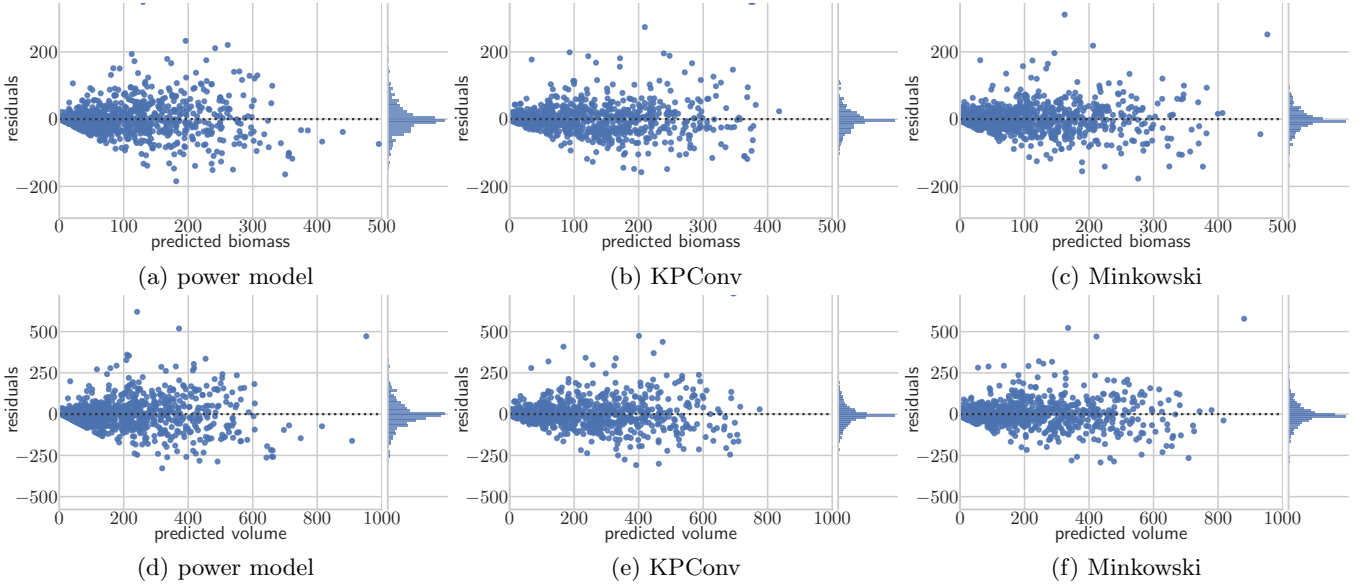


Figure 8: Residual (left side) and error distribution (right side) plots of the test performance for the power regression, KPConv, and the Minkowski model. The first row shows errors for AGB and the second for wood volume. The other models are shown in the supplementary material (see Figure A.2).

The RF performed the worst. The better performance of the linear regression with an R^2 of 0.757 for biomass and 0.760 for wood volume, indicates that the calculated features are indeed linearly correlated with the targets. The power regression model based on [MNLRN18] reaches R^2 values of 0.761 and 0.763 for biomass and tree volume, respectively, that is, the deep learning approach clearly improved over the state-of-the-art method. All three point cloud based methods outperformed the models based on the precomputed features, justifying that the networks indeed utilized additional information from the point clouds. The MAPE, which was not an optimization criterion, shows the largest differences between the methods, which are mainly due to errors related to small target values.

The national forest inventory data offers the fraction of conifer and broadleaf for each site, which we used to analyze the performance at different fractions in Figure 7. Interestingly, KPConv performs better than the Minkowski model for conifer fraction interval $(0, 33]$ and 100. Again, the high MAPE for the methods based on the precomputed features is noticeable, in particular when a mono culture is analyzed. In general, mono cultures turned out to be more difficult than mixed forests w.r.t. MAPE and forests with conifer trees exhibit a lower RMSE.

Figure 8 illustrates residual plots and error distribution of biomass and wood volume, respectively. The spread of errors increases with magnitude of the target variables. While low values are more overestimated, high values tend to be more underestimated. Comparing the dis-

tribution of errors of the assessed models, one can see that the KPConv and Minkowski model display generally lower spread of errors.

Quantitative comparison to other studies. Caution is warranted when comparing our prediction accuracy with in other studies. Reported errors of ALS-based prediction models for AGB range from 17 to 40 Mg C ha⁻¹ in the tropics [AHM⁺11], and this error is comparable to estimates reported in other regions as well [LCH⁺02]. It is reassuring that we achieve error rates at the lower end of this spectrum. However, it is important to stress that is not uncommon that the indicators documented in these studies measure the error on the training data set as a goodness of fit index (e.g., in [LHC⁺99] the R^2 for AGB drops from 80% down to 33% when the model is applied to a different data set). The training errors of our models are even lower than the test set results in Table 1 (see Table A.1 in the supplementary material).

It has been found that the errors of ALS-based carbon stock estimates decrease with increasing the spatial resolution [MDAML11, FSMM16]. It has been hypothesized that the RMSE of the standard methods scales with the inverse square root of the study area [MDAML11] (e.g., in [MDAML11], the RMSE of the estimated density decreased from 63.2 to 6.5 Mg C ha⁻¹ when the spatial resolution is increased from 0.04 to 6.25 ha). Our study areas are of size $a = 15^2 \cdot \pi \cdot 10^{-4}$ ha ≈ 0.07 ha.

Simply applying the formula by [MDAML11] would predict a $1 - 1/\sqrt{a^{-1}} = 1 - \sqrt{a} \approx 73\%$ lower RMSE (5.362 Mg C ha⁻¹ for the Minkowski model) at 1 ha resolution. The residual shown in Figure 8 indeed suggest that our errors would average out if several subplots were combined in the error computation.

6 Conclusions

Reducing the uncertainty of biomass stocks contained in forests is important for understanding the global carbon budget and how it circulates between land and the atmosphere [ZGD13] (e.g., the estimates can be used to calibrate coupled climate-carbon cycle models). More precise knowledge of forest biomass development is needed to study the processes driving af-, re-, and deforestation. This, in turn, is a requisite for achieving the United Nations Strategic Plan for Forests under the Paris agreement [UN 2021; UN 2017; IPCC 2018).

This study brings forward deep learning systems for predicting above-ground biomass, wood volume, and carbon storage in forests directly from LiDAR point clouds. We modified existing neural network architectures for classification to perform regression and evaluated them on a unique data set combining field measurements and air-

borne LiDAR data. Our adaptation of Minkowski CNNs gave the best results. This approach uses an efficient implementation of 3D convolutions for sparse data. That is, it basically relies on the same operations as CNNs for standard 2D and 3D image processing in contrast to the other methods we evaluated.

We achieved high accuracies, considerably better than the state-of-the-art approach operating on basic statistics of the point clouds. The coefficient of determination R^2 for above-ground biomass and stored carbon exceeded 0.83 on a test set not considered in the modelling process. These encouraging results may be the first step towards a paradigm shift in the methodology for analyzing LiDAR data for terrestrial ecosystem analysis.

References

- [AH11] Raf Aerts and Olivier Honnay. Forest restoration, biodiversity and ecosystem functioning. *BMC Ecology*, 11(1):1–10, 2011. 1
- [AHM⁺11] Gregory P. Asner, R. Flint Hughes, Joseph Mascaro, Amanda L. Uowolo, David E. Knapp, James Jacobson, Ty Kennedy-Bowdoin, and John K. Clark. High-resolution carbon mapping on the million-hectare island of Hawaii. *Frontiers in Ecology and the Environment*, 9(8):434–439, 2011. 9
- [Bre01] Leo Breiman. Random forests. *Machine learning*, 45(1):5–32, 2001. 7
- [CFG⁺15] Angel X. Chang, Thomas A. Funkhouser, Leonidas J. Guibas, Pat Hanrahan, Qi-Xing Huang, Zimo Li, Silvio Savarese, Manolis Savva, Shuran Song, Hao Su, Jianxiong Xiao, Li Yi, and Fisher Yu. Shapenet: An information-rich 3d model repository. *CoRR*, abs/1512.03012, 2015. 4
- [CGS19] Christopher Choy, JunYoung Gwak, and Silvio Savarese. 4D spatio-temporal convnets: Minkowski convolutional neural networks. In *CVPR*, pages 3075–3084, 2019. 2, 4, 5
- [CNHL20] Thomas Chaton, Chaulet Nicolas, Sofiane Horache, and Loic Landrieu. Torch-Points3D: A modular multi-task framework for reproducible deep learning on 3D point clouds. In *3D Vision (3DV)*. IEEE, 2020. 4
- [CPB⁺06] Jean-Michel Carnus, John Parrotta, Eckehard Brockerhoff, Michel Arbez, Hervé Jactel, Antoine Kremer, David Lamb, Kevin O’Hara, and Bradley Walters. Planted forests and biodiversity. *Journal of Forestry*, 104(2):65–77, 2006. 1
- [CUH16] Djork-Arné Clevert, Thomas Unterthiner, and Sepp Hochreiter. Fast and accurate deep network learning by exponential linear units (ELUs). In *ICLR*, 2016. 5

- [EKP⁺18] Karl-Heinz Erb, Thomas Kastner, Christoph Plutzer, Anna Liza S Bais, Nuno Carvalhais, Tamara Fetzl, Simone Gingrich, Helmut Haberl, Christian Lauk, Maria Niedertscheider, Julia Pongratz, Martin Thurner, and Sebastiaan Luyssaert. Unexpectedly large impact of forest management and grazing on global vegetation biomass. *Nature*, 553(7686):73–76, 2018. 1
- [FSMM16] António Ferraz, Sassan Saatchi, Clément Mallet, and Victoria Meyer. Lidar detection of individual tree size in tropical forests. *Remote Sensing of Environment*, 183:318–333, 2016. 9
- [FTS⁺15] Sandro Federici, Francesco N. Tubiello, Mirella Salvatore, Heather Jacobs, and Josef Schmidhuber. New estimates of CO2 forest emissions and removals: 1990–2015. *Forest Ecology and Management*, 352:89–98, 2015. 1
- [FVA⁺21] Ahmet Frintepe, Carolin Vey, Stylianos Asteriadis, Alain Pagani, and Didier Stricker. From IR images to point clouds to pose: Point cloud-based AR glasses pose estimation. *Journal of Imaging*, 7(5), 2021. 2
- [GAE⁺17] Bronson W. Griscom, Justin Adams, Peter W. Ellis, Richard A. Houghton, Guy Lomax, Daniela A. Miteva, William H. Schlesinger, David Shoch, Juha V. Siikamäki, Pete Smith, Peter Woodbury, Chris Zganjar, Allen Blackman, João Campari, Richard T. Conant, Christopher Delgado, Patricia Elias, Trisha Gopalakrishna, Marisa R. Hamsik, Mario Herrera, Joseph Kiesecker, Emily Landis, Lars Laestadius, Sara M. Leavitt, Susan Minnemeyer, Stephen Polasky, Peter Potapov, Francis E. Putz, Jonathan Sanderman, Marcel Silvius, Eva Wollenberg, and Joseph Fargione. Natural climate solutions. *Proceedings of the National Academy of Sciences*, 114(44):11645–11650, 2017. 1
- [GCC06] Nicholas R Goodwin, Nicholas C Coops, and Darius S Culvenor. Assessment of forest structure with airborne lidar and the effects of platform altitude. *Remote Sensing of Environment*, 103(2):140–152, 2006. 2
- [GEVDM18] Benjamin Graham, Martin Engelcke, and Laurens Van Der Maaten. 3D semantic segmentation with submanifold sparse convolutional networks. In *CVPR*, pages 9224–9232, 2018. 5
- [Gir15] Ross Girshick. Fast R-CNN. In *ICCV*, pages 1440–1448, 2015. 7
- [Gra15] Ben Graham. Sparse 3D convolutional neural networks. In *BMVC*, 2015. 5
- [GRY18] Lihao Ge, Zhou Ren, and Junsong Yuan. Point-to-point regression PointNet for 3D hand pose estimation. In *ECCV*, pages 475–491, 2018. 2
- [Hou05] Richard A. Houghton. Aboveground forest biomass and the global carbon balance. *Global Change Biology*, 11(6):945–958, 2005. 1
- [HPM⁺13] Matthew C. Hansen, Peter V. Potapov, Rebecca Moore, Matt Hancher, Svetlana A. Turubanova, Alexandra Tyukavina, David Thau, Stephen V. Stehman, Scott J. Goetz, Thomas R. Loveland, et al. High-resolution global maps of 21st-century forest cover change. *Science*, 342(6160):850–853, 2013. 1
- [HSL⁺17] Timo Hackel, Nikolay Savinov, Lubor Ladicky, Jan Dirk Wegner, Konrad Schindler, and Marc Pollefeys. Semantic3d.net: A new large-scale point cloud classification benchmark. *CoRR*, abs/1704.03847, 2017. 4
- [HSS18] Jie Hu, Li Shen, and Gang Sun. Squeeze-and-excitation networks. In *CVPR*, 2018. 5, 7
- [JHF17] Rasmus Jensen, Mathias Herbst, and Thomas Friborg. Direct and indirect controls of the inter-annual variability in atmospheric CO2 exchange of three contrasting ecosystems in Denmark. *Agricultural and Forest Meteorology*, 233:12–31, 2017. 1
- [Joh99] Vivian Kvist Johannsen. *A growth model for oak in Denmark*. PhD thesis, Royal Veterinary and Agricultural University, Copenhagen, Denmark, 1999. 3
- [Kis98] Leslie Kish. Space/time variations and rolling samples. *Journal of Official Statistics*, 14(1):31, 1998. 3
- [KN17] René Kemp and Babette Never. Green transition, industrial policy, and economic development. *Oxford Review of Economic Policy*, 33(1):66–84, 2017. 1
- [LCH⁺02] Michael A. Lefsky, Warren B. Cohen, David J. Harding, Geoffrey G. Parker, Steven A. Acker, and S. Thomas Gower. Lidar remote sensing of above-ground biomass in three biomes. *Global Ecology and Biogeography*, 11(5):393–399, 2002. 9
- [LH17] Ilya Loshchilov and Frank Hutter. SGDR: stochastic gradient descent with warm restarts. In *ICLR*. OpenReview.net, 2017. 7
- [LH19] Ilya Loshchilov and Frank Hutter. Decoupled weight decay regularization. In *ICLR*. OpenReview.net, 2019. 7
- [LHC⁺99] Michael A. Lefsky, D. Harding, W. B. Cohen, G Parker, and H. H. Shugart. Surface lidar remote sensing of basal area and biomass in deciduous forests of eastern maryland, usa. *Remote Sensing of Environment*, 67(1):83–98, 1999. 2, 9
- [LOH⁺11] Bruce Lippke, Elaine Oneil, Rob Harrison, Kenneth Skog, Leif Gustavsson, and Roger Sathre. Life cycle impacts of forest management and

- wood utilization on carbon mitigation: knowns and unknowns. *Carbon Management*, 2(3):303–333, 2011. 1
- [LWMK19] Simon L Lewis, Charlotte E Wheeler, Edward TA Mitchard, and Alexander Koch. Regenerate natural forests to store carbon. *Nature*, 568(7750):25–28, 2019. 1
- [McD03] Trent L. McDonald. Review of environmental monitoring methods: survey designs. *Environmental Monitoring and Assessment*, 85(3):277–292, 2003. 3
- [MDAML11] Joseph Mascaro, Matteo Detto, Gregory P. Asner, and Helene C. Muller-Landau. Evaluating uncertainty in mapping forest carbon with airborne LiDAR. *Remote Sensing of Environment*, 115(12):3770–3774, 2011. 2, 9
- [MNLRN18] Steen Magnussen, Thomas Nord-Larsen, and Torben Riis-Nielsen. Lidar supported estimators of wood volume and aboveground biomass from the Danish national forest inventory (2012–2016). *Remote Sensing of Environment*, 211:146–153, 2018. 2, 6, 7, 8
- [MRMV⁺15] Stéphane Mermoz, Maxime Réjou-Méchain, Ludovic Villard, Thuy Le Toan, Vivien Rossi, and Sylvie Gourlet-Fleury. Decrease of l-band sar backscatter with biomass of dense forests. *Remote Sensing of Environment*, 159:307–317, 2015. 2
- [MSW⁺12] Edward T. A. Mitchard, Sassan S. Saatchi, Lee J. T. White, Katharine Anne Abernethy, Kathryn Jane Jeffery, Simon L. Lewis, Murray Collins, Michael A. Lefsky, Miguel E. Leal, Iain H. Woodhouse, and Patrick Meir. Mapping tropical forest biomass with radar and spaceborne LiDAR in Lopé National Park, Gabon: overcoming problems of high biomass and persistent cloud. *Biogeosciences*, 9(1):179–191, 2012. 2
- [Næs09] Erik Næsset. Effects of different sensors, flying altitudes, and pulse repetition frequencies on forest canopy metrics and biophysical stand properties derived from small-footprint airborne laser data. *Remote Sensing of Environment*, 113(1):148–159, 2009. 2
- [Näs36] Manfred Näslund. Skogsförsöksanstaltens gallringsförsök i tallskog. *Meddelanden från Statens skogsförsöksanstalt*, 29:1–169, 1936. 3
- [NDB⁺07] Bert Netz, Ogunlade R. Davidson, Peter R. Bosch, Rutu Dave, and Leo A. Meyer. Climate change 2007: Mitigation. Contribution of Working Group III to the fourth assessment report of the intergovernmental panel on climate change. Summary for policymakers. *Climate change 2007: Mitigation. Contribution of Working Group III to the Fourth Assessment Report of the Intergovernmental Panel on Climate Change. Summary for Policymakers*, 2007. 1
- [NLJ16] Thomas Nord-Larsen and Vivian Kvist Johannsen. Danish national forest inventory: Design and calculations. *IGN Report, Department of Geosciences and Natural Resource Management, University of Copenhagen*, 2016. 2
- [NLMS17] Thomas Nord-Larsen, Henrik Meilby, and Jens Peter Skovsgaard. Simultaneous estimation of biomass models for 13 tree species: effects of compatible additivity requirements. *Canadian J. of Forest Research*, 47(6):765–776, 2017. 3
- [NLRNO17] Thomas Nord-Larsen, Torben Riis-Nielsen, and Mathias Bo Ottosen. Forest resource map of Denmark: Mapping of Danish forest resource using ALS from 2014–2015. *IGN Report, Department of Geosciences and Natural Resource Management, University of Copenhagen*, 2017. 6
- [Ope17] OpenStreetMap contributors. Planet dump retrieved from <https://planet.osm.org>. <https://www.openstreetmap.org>, 2017. 2
- [OSE⁺99] Anthony R. Olsen, Joseph Sedransk, Don Edwards, Carol A. Gotway, Walter Liggett, Stephen Rathbun, Kenneth H. Reckhow, and Linda J. Yyoung. Statistical issues for monitoring ecological and natural resources in the united states. *Environmental Monitoring and Assessment*, 54(1):1–45, 1999. 3
- [PGM⁺19] Adam Paszke, Sam Gross, Francisco Massa, Adam Lerer, James Bradbury, Gregory Chanan, Trevor Killeen, Zeming Lin, Natalia Gimelshein, Luca Antiga, et al. Pytorch: An imperative style, high-performance deep learning library. *NeurIPS*, 32:8026–8037, 2019. 7
- [PVG⁺11] Fabian Pedregosa, Gaël Varoquaux, Alexandre Gramfort, Vincent Michel, Bertrand Thirion, Olivier Grisel, Mathieu Blondel, Peter Prettenhofer, Ron Weiss, Vincent Dubourg, Jake Vanderplas, Alexandre Passos, and David Cournapeau. Scikit-learn: Machine learning in Python. *Journal of Machine Learning Research*, 12:2825–2830, 2011. 7
- [QSMG17] Charles R. Qi, Hao Su, Kaichun Mo, and Leonidas J. Guibas. PointNet: Deep learning on point sets for 3D classification and segmentation. In *CVPR*, pages 652–660, 2017. 2, 4
- [SGM93] Branislav Sloboda, Dieter Gaffrey, and Naoto Matsumura. Regionale und lokale Systeme von Höhenkurven für gleichaltrige Waldbestände. *Allgemeine Forst-und Jagdzeitung*, 164(12):225–228, 1993. 3
- [SJSN15] Suman Sinha, Chockalingam Jeganathan, Laxmi Kant Sharma, and Mahendra Singh Nathawat. A review of radar remote sensing for biomass estimation. *Int. Journal of Environmental Science and Technology*, 12(5):1779–1792, 2015. 2

- [SM12] Taishichirō Satoo and HA Madgwick. *Forest biomass*, volume 6. Springer Science & Business Media, 2012. 1
- [TMMM09] Ian Thompson, Brendan Mackey, Steven McNulty, and Alex Mosseler. Forest resilience, biodiversity, and climate change. In *Secretariat of the Convention on Biological Diversity*, volume 43 of *Montreal Technical Series*, pages 1–67, 2009. 1
- [TQD⁺19] Hugues Thomas, Charles R. Qi, Jean-Emmanuel Deschaud, Beatriz Marcotegui, François Goulette, and Leonidas J. Guibas. KPConv: Flexible and deformable convolution for point clouds. *ICCV*, pages 6411–6420, 2019. 2, 4, 5
- [WSK⁺15] Zhirong Wu, Shuran Song, Aditya Khosla, Fisher Yu, Linguang Zhang, Xiaoou Tang, and Jianxiong Xiao. 3d shapenets: A deep representation for volumetric shapes. In *CVPR*, pages 1912–1920. IEEE Computer Society, 2015. 4
- [ZGD13] Scott G. Zolkos, Scott J. Goetz, and Ralph Dubayah. A meta-analysis of terrestrial above-ground biomass estimation using lidar remote sensing. *Remote Sensing of Environment*, 128:289–298, 2013. 2, 9
- [ZYTCS03] Wenyang Zhang, Qiwei Yao, Howell Tong, and Nils Chr. Stenseth. Smoothing for spatiotemporal models and its application to modeling Muskrat-Mink interaction. *Biometrics*, 59(4):813–821, 2003. 3

A Supplementary Material

In the following, we will give more results as well as notes on how to reproduce these results.

A.1 Additional Results

We present the results on the training and validation set in Table A.1 and A.2, respectively. Note that the extracted features models (lin. model, power model, and RF) were also trained on the validation set, while our point cloud regression models were not. Still, the models directly working on the point cloud data produced better results.

The errors for changing fractions of conifer and broadleaf trees for wood volume are shown in Figure A.1. Results are similar to the ones concerning biomass (see Figure 7). Further, the residual and error distribution plots for the lin., RF, and PointNet models are shown in Figure A.2. It seems underpredictions in the RF model for higher biomass contributed most to its sub-par performance.

In Figure A.3 we show more subplots with particularly low or high values for above-ground biomass. For example, the first two subplots have low AGB with 1.79 and 1.89 Mg ha⁻¹, which is reflected by the sparse vegetation in the point cloud. This is difficult to capture with commonly used statistics derived from point cloud data, and therefore models based on these features (e.g., RF, lin., and power model) overestimated. Interestingly, PointNet also overestimate values due to the employed global aggregation without intermediate downsampling steps (similar to global feature extraction). The third example in Figure A.3 exhibits a high AGB value with 417.60 Mg ha⁻¹ and the point cloud shows a densely populated and natural broadleaf forest. Again, this is difficult to estimate since the derived statistics do not offer information about individual biomass contributions and thus most methods underestimate them. The fourth subplots biomass is 245.89 Mg ha⁻¹ from a conifer forest and the predictions align well with the target. We also give a visualization of the plots and subplots in Figure A.4 (as described in Section 2).

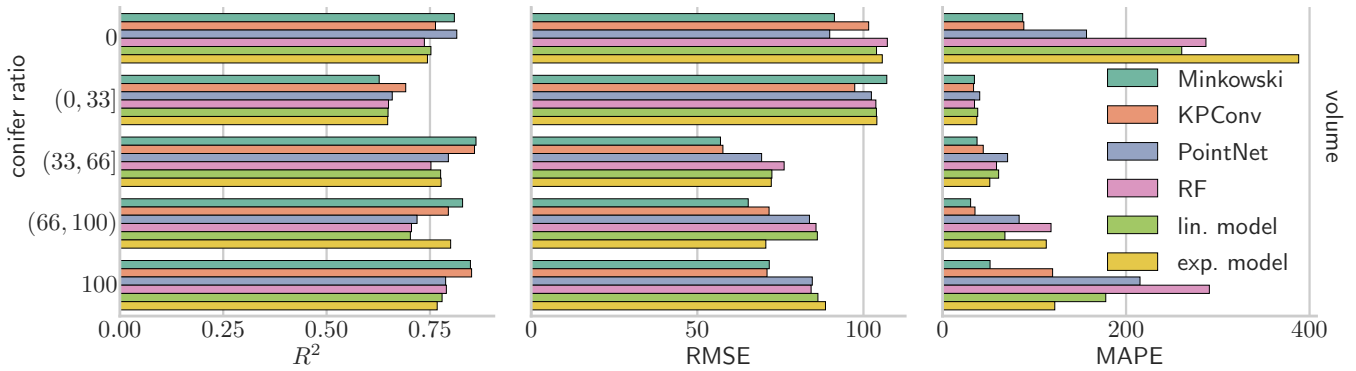


Figure A.1: Errors for different fractions of conifer and broadleaf trees for wood volume. The columns show R^2 , RMSE, and MAPE.

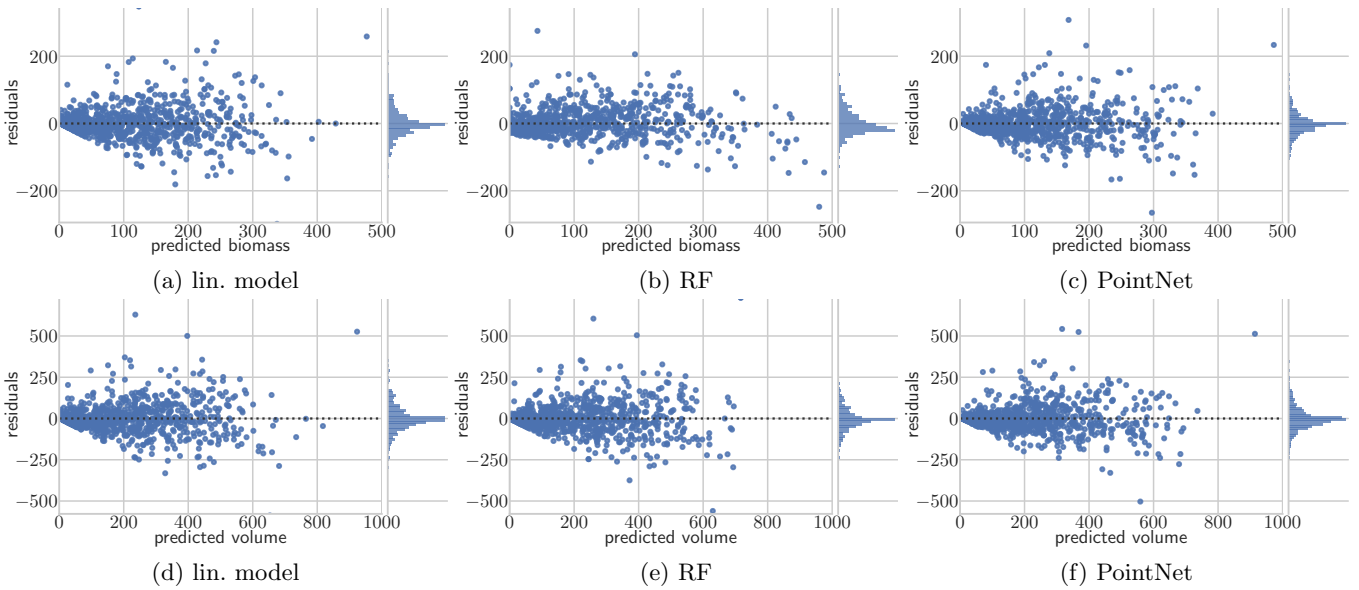
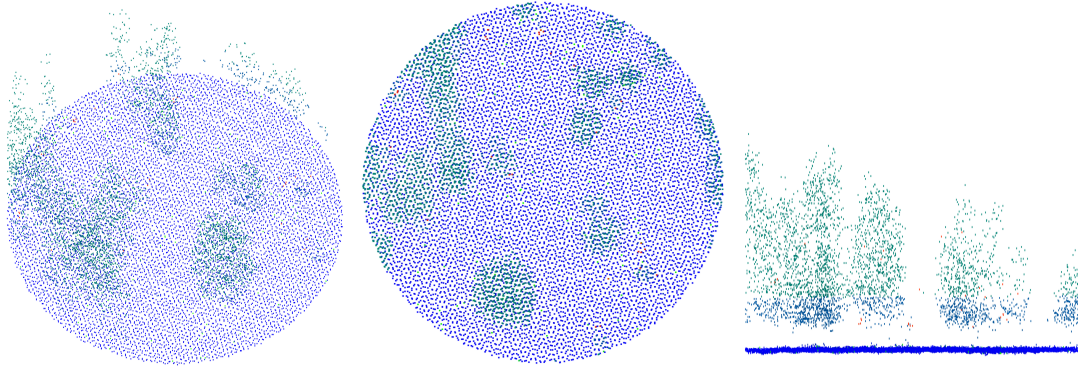
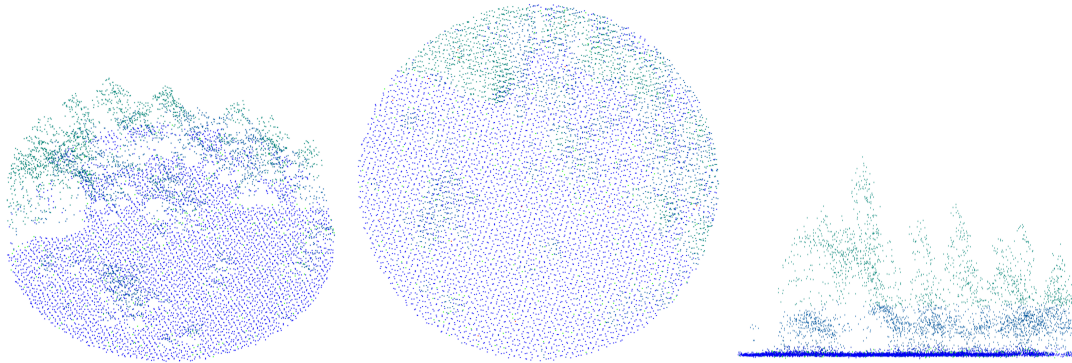


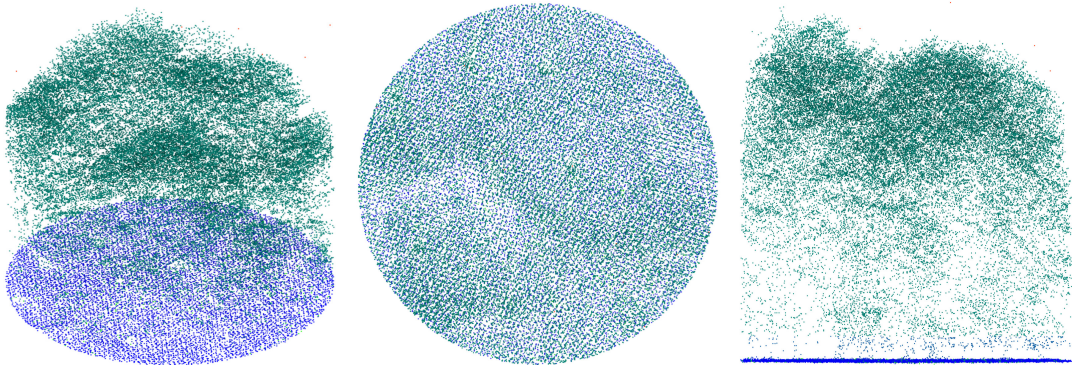
Figure A.2: Residual (left side) and error distribution (right side) plots of the test performance for the lin. regression, RF, and the PointNet model. The first row shows errors for biomass and the second for wood volume.



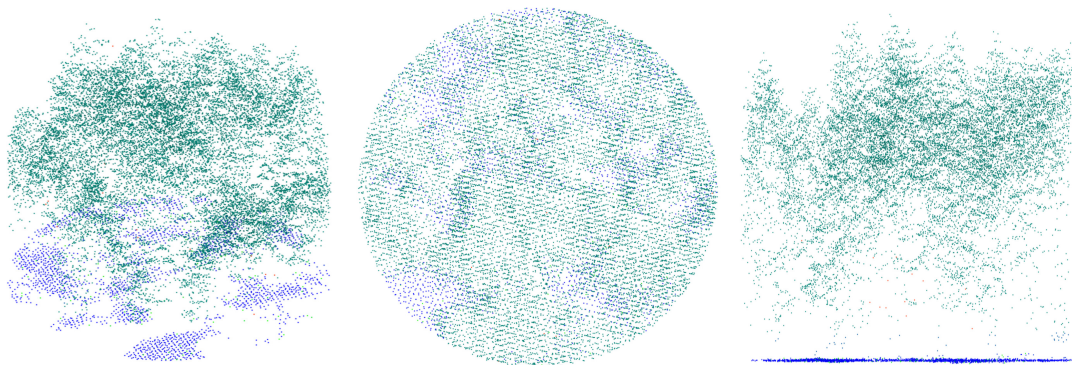
(a) Target: 1.79; Minkowski: 1.59; KPConv: 3.16; PointNet: 10.17; RF: 8.70, lin. model: 10.42; power model: 11.31



(b) Target: 0.86; Minkowski: 1.00; KPConv: 3.99; PointNet: 11.31; RF: 7.00, lin. model: 8.09; power model: 9.94



(c) Target: 417.60; Minkowski: 345.71; KPConv: 381.54; PointNet: 298.25; RF: 285.75, lin. model: 272.74; power model: 270.98



(d) Target: 245.90; Minkowski: 212.94; KPConv: 273.01; PointNet: 195.50; RF: 216.13, lin. model: 212.38; power model: 217.86



3

Figure A.3: More examples of subplots in each row with three perspectives: isometric front, top, and side view. Each subplots caption contains the measured and estimated biomass in Mg ha^{-1} .

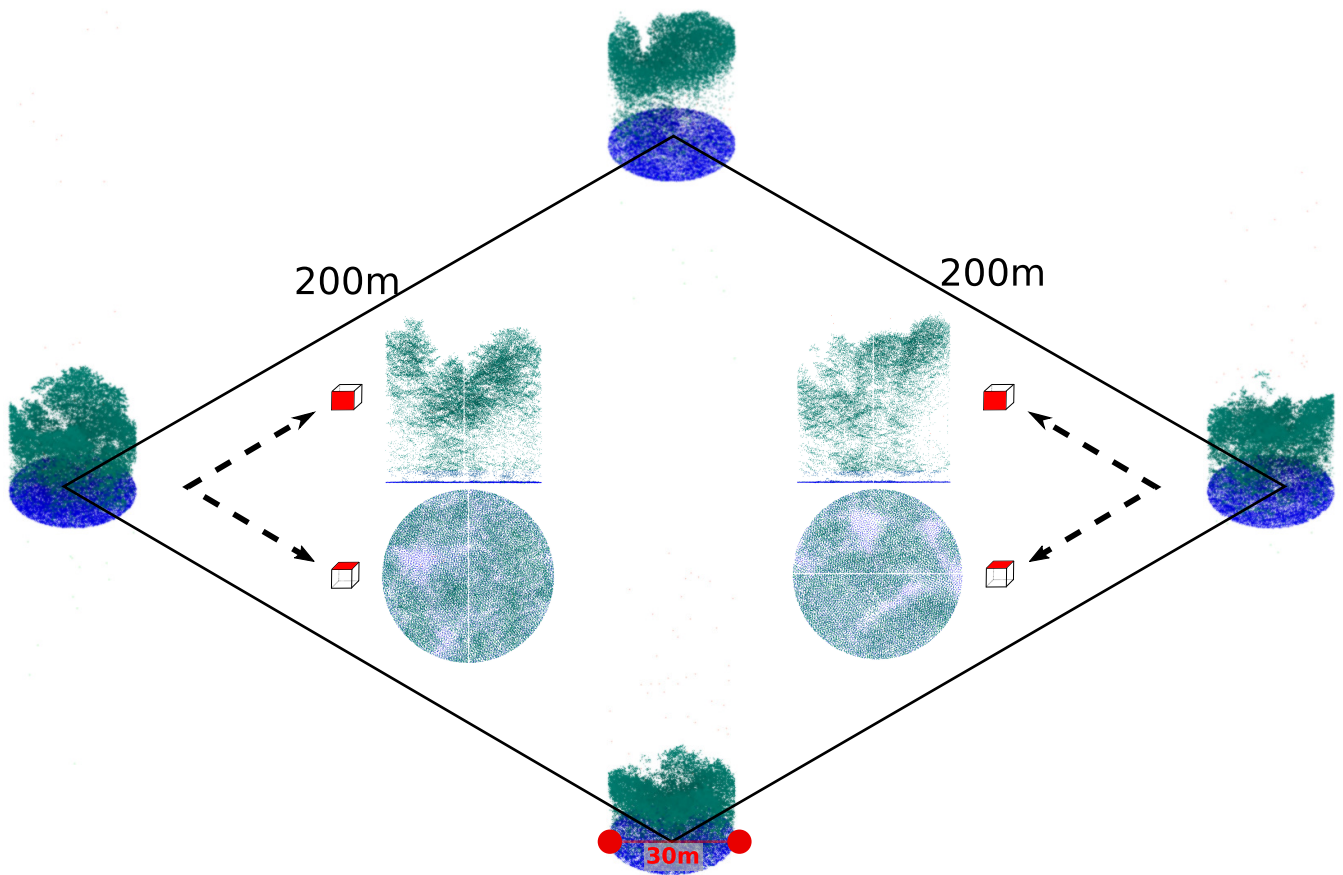


Figure A.4: One plot sample from a 2×2 km area as described in Section 2. Each plot usually contains four point cloud subplots in a 200×200 m square. All LiDAR subplots have a diameter of 30 m and their own biomass as well as wood volume measurements.

Table A.1: Comparison of methods showing the R^2 score, RMSE, and MAPE on the train set. The R^2 and MAPE for biomass are the same as for carbon. Note that we excluded 0 biomass measurements from MAPE to avoid numerical issues. Best results are highlighted.

target	model	R^2	RMSE	MAPE
AGB	lin. model	0.712	55.473	793.650
	power model	0.700	56.633	635.976
	RF	0.759	50.733	581.331
	PointNet	0.779	48.626	574.688
	KPConv	0.833	42.297	288.671
	Minkowski	0.823	43.557	143.766
volume	lin. model	0.716	103.515	192.794
	power model	0.703	105.835	187.629
	RF	0.765	94.117	162.380
	PointNet	0.780	91.042	145.557
	KPConv	0.832	79.697	81.628
	Minkowski	0.823	81.739	62.348

Table A.2: Comparison of methods showing the R^2 score, RMSE, and MAPE on the validation set. The R^2 and MAPE for biomass are the same as for carbon. Note that we excluded 0 biomass measurements from MAPE to avoid numerical issues. Best results are highlighted. Note that the deep learning models did not train on this data directly but the feature extraction methods did.

target	model	R^2	RMSE	MAPE
AGB	lin. model	0.736	54.368	412.068
	power model	0.739	54.005	334.801
	RF	0.775	50.123	422.567
	PointNet	0.776	50.034	374.804
	KPConv	0.786	48.975	309.796
	Minkowski	0.805	46.654	113.969
volume	lin. model	0.764	95.053	117.857
	power model	0.766	94.631	111.389
	RF	0.801	87.395	115.147
	PointNet	0.804	86.719	104.459
	KPConv	0.812	84.860	78.257
	Minkowski	0.823	82.463	60.135